Charge Transport in TiO_2 Films With Complex Percolation Pathways Investigated by Time-Resolved Terahertz Spectroscopy

H. Němec, V. Zajac, I. Rychetský, D. Fattakhova-Rohlfing, B. Mandlmeier, T. Bein, Z. Mics, and P. Kužel

(Invited Paper)

***Abstract*—The depolarization fields play an important role in terahertz experiments on nanostructured samples with complex nanoparticle morphologies and percolation pathways. Namely, their effects can hide or distort peculiarities of nanoscopic charge transport in the spectra measured on these structures. We calculate the local fields for a large number of percolated and non-percolated two-dimensional model structures by numerical solving of Maxwell equations in the quasi-static limit. The results strongly suggest that in a broad family of structures a simple effective medium approximation model can be applied to characterize the effective response. The model consists in an equivalent circuit composed of a resistance accounting for the percolated chains with an additional parallel RC-branch describing the non-percolated part. The physical meaning of this model is discussed in the frame of the Bergman spectral representation of effective medium. We show a recipe for the retrieval of a response connected to the depolarization fields and to the nanoscale transport mechanisms from transient terahertz spectra. Finally, we use the model to interpret our THz photoconductivity spectra in various TiO_2 films with nanofabricated percolation pathways.**

***Index Terms*— Charge carrier mobility, mesoporous materials, photoconductivity, semiconductor nanostructures.**

I. Introduction

THE time-resolved terahertz spectroscopy is an experimental tool par excellence for studying ultrafast conductivity and initial stages of the carrier transport in nanostructured semiconductors or in semiconductors disordered on the nanoscale [1]–[3]. Such semiconducting systems are linked to a wide range of important industrial applications: fast conductivity in amorphous and nanocrystalline silicon [4]–[6], in organic semiconductors [7], graphene [8] and in dye-sensitized semiconductor nanoparticles [9] was investigated in an effort to achieve low-cost, easy-fabrication devices for photovoltaic and optoelectronic applications (solar cells, thin-film transistors, light-emitting diodes, etc.) [3], [10]. The absence of long-range crystal order fundamentally complicates the charge transport in these materials.

In the terahertz regime, a subpicosecond time resolution can be achieved and the transport of charges over units to several tens of nanometers is mainly probed. These are quite appropriate time and length scales of ultrafast carrier trapping at nanocrystal surface states and short range transport inside and among individual nanocrystals. In addition, a non-contact fashion of carrier injection and probing allows one to overcome a number of experimental difficulties.

The basic results of optical pump—terahertz probe experiments [11] are complex photoconductivity spectra in the terahertz range, which usually vary as a function of the pump-probe delay τ_p : $\Delta\sigma(\omega,\tau_p) = \Delta\sigma' + i\Delta\sigma''$. The spectral behavior of this complex response function is crucial for understanding the conductivity mechanisms and the degree of charge localization. To get an intuitive insight into the problem an analogy can be found with simple electrical circuits [2]. The response of delocalized carriers is characterized by a self-inductance L which describes the inductive screening of the applied field, while the energy loss of carriers due to scattering is described by a resistance R. The complex conductivity of this process is then proportional to the admittance of their serial connection: $\Delta\sigma \propto (R - i\omega L)^{-1}$; note that this expression is equivalent to the Drude conductivity formula with a momentum scattering time equal to L/R. Hence $\Delta\sigma''$ of delocalized carriers always exhibits a positive sign (inductive response) and $\Delta\sigma'$ decreases with frequency. For localized carriers, the polarization created by the carrier transport takes over the induction and an essentially capacitive character of the response is obtained with a negative imaginary part and a positive increasing real part of the conductivity: $\Delta\sigma \propto (R + i/\omega C)^{-1}$. Within this analogy a superposition of several conductivity mechanisms (e.g. populations of delocalized and localized carriers which are spatially separated or carrier–exciton system) can be described by circuits connected in parallel.

Manuscript received February 07, 2013; revised March 20, 2013; accepted March 20, 2013. Date of publication April 15, 2013; date of current version April 29, 2013. This work was supported by the Academy of Sciences of the Czech Republic under Project M100101218 and by the Czech Science Foundation under Grant 13-12386S . The work of V. Zajac. was supported by the Granting Agency of the Charles University under project GAUK 539612. The work of I. Rychetský was supported by the Czech Science Foundation under Grant P204/12/0232. The work of D. Fattakhova-Rohlfing, B. Mandlmeier, and T. Bein was supported by the German Research Foundation (DFG) under Grant FA 839/1-2, by Nanosystems Initiative Munich (NIM), and by LMUexcellent and LMUmentoring funded by the DFG.

H. Němec, I. Rychetský, and P. Kužel are with the Institute of Physics, Academy of Sciences of the Czech Republic, 18221 Prague 8, Czech Republic (e-mail: kuzelp@fzu.cz).

V. Zajac is with the Institute of Physics, Academy of Sciences of the Czech Republic, 18221 Prague 8, Czech Republic, and also with the Faculty of Mathematics and Physics, Charles University in Prague, 12116 Prague 2, Czech Republic.

D. Fattakhova-Rohlfing, B. Mandlmeier, and T. Bein are with Department of Chemistry and Center for NanoScience, University of Munich, 81377 Munich, Germany.

Z. Mics is with the Max Planck Institute for Polymer Research, 55128 Mainz, Germany.

Color versions of one or more of the figures in this paper are available online at http://ieeexplore.ieee.org.

Digital Object Identifier 10.1109/TTHZ.2013.2255555

A more detailed picture of the charge transport and dynamics can be obtained by means of a suitable microscopic model which needs to be confronted with the experimental data. However, we emphasize that the measured spectra represent a macroscopic response $\Delta\sigma$ of the sample which can, in principle, substantially differ from the microscopic one, $\Delta\sigma_{\mathrm{mic}}$. This is due to an inherently inhomogeneous nature of the sample composed of nanoparticles or containing complex percolation pathways. We define a microscopic mobility of a charge carrier μ as a microscopic conductivity per single unit charge. This is a response function of the carrier to the local electric field at the place where the charge is actually located. In the experiment, the quantum yield ξ of photoexcited carriers is frequently not a priori known with precision and, consequently, it is difficult to evaluate directly the photocarrier concentration N without any additional assumptions; on the other hand, the measurement of the pump fluence incident on the sample provides the number of excitations (absorbed photons) N_{exc} per laser pulse and per unit volume. We introduce so called yield-mobility product:

$$\xi\mu = \frac{\Delta\sigma_{\mathrm{mic}}}{eN_{\mathrm{exc}}}. \tag{1}$$

In many experimental conditions, when the measured ultrafast dynamics is not faster than the probing THz pulse length, the following proportionality holds [4], [12]:

$$\Delta\sigma(\omega,\tau_p) \propto -\frac{\Delta E(\omega,\tau_p)}{E(\omega)} \tag{2}$$

where ΔE is the transient transmitted THz spectrum (induced by the photoexcitation) and E is the transmitted signal through the sample without excitation. In the case of probing a thin photoexcited layer one obtains more specifically [12], [13]

$$\frac{\Delta\sigma}{eN_{\mathrm{exc}}} = -\frac{(n_1+n_2)}{z_0}\frac{1}{e\phi}\frac{\Delta E}{E} \tag{3}$$

where n_1 and n_2 are the refractive indices of the media surrounding the photoexcited layer, z_0 is the vacuum wave impedance and ϕ is the photon fluence (in cm^{-2}) entering the sample and absorbed ($\phi = F/h\nu$ where F is the pump energy fluence in $\mathrm{J/cm}^2$). By comparing (1) and (3) one concludes that the left-hand side of (3) is equal to the yield-mobility product if the depolarization fields can be neglected. In this case the yield-mobility product can be reliably determined from the experimental spectra. The right-hand side of (3) will be very frequently used in our theoretical and experimental analysis; for this reason we introduce a new quantity ΔX_σ proportional to the transient transmission of a thin film:

$$\Delta X_\sigma = -\frac{(n_1+n_2)}{z_0}\frac{1}{e\phi}\frac{\Delta E}{E}. \tag{4}$$

In the simplest case described by (3), ΔX_σ is simply equal to the normalized macroscopic conductivity. We will show later in this paper that this relation may become more complicated due to depolarization fields and ΔX_σ will be related to the photoconductivity integrated over the excited layer. For this reason we call this quantity normalized transient sheet conductivity.

The interpretation of experimental data should encompass both the local fields in an inhomogeneous sample and the charge carrier response function μ. Our point is that the description of the two phenomena should be divided into separate steps and the task of the experimenter is then twofold:

i) To develop a model able to transform correctly the measured macroscopic conductivity $\Delta\sigma$ to the microscopic response function μ; this model is usually based on some kind of effective medium approximation and consists in an evaluation of the depolarization fields in the inhomogeneous sample which are at the origin of the difference between the applied THz probing field and the local field acting on charge carriers. In the case of isolated photoconductive inclusions these phenomena can be described with the help of the concept of localized plasmons [13]. In a more general case such a model should take into account the form and filling fraction of the crystalline phase in the sample and possibly also the percolation pathways of its photoconductive parts.

ii) To describe and understand the transport mechanism on a nanoscopic scale based on the spectra of μ. The description of $\mu(\omega)$ can be based e.g. on the Drude or Drude–Lorentz models or on their phenomenological extensions like the Drude model modified by the distribution of scattering times [14] or the Drude–Smith model [15], [16]. Alternatively, more elaborate microscopic models can be developed and applied; we proposed, e.g., Monte Carlo simulations of carriers scattered on nanocrystalline boundaries [17], [18] or moving in an external potential [19]. A comprehensive review of available models has been published recently [2].

These important assessments cannot be made in any way from a single spectrum. Indeed, photoconductivity spectra can be experimentally determined for several temperatures T and especially as a function of the photocarrier concentration $N = \xi N_{\mathrm{exc}}$ over at least one order of magnitude; these two parameters are easily experimentally controllable and knowledge of the photoconductivity spectra for various N and T usually provides a much deeper insight into the underlying mechanisms. The magnitude of the permittivity change in the photoexcited parts of the sample

$$\Delta\varepsilon = \frac{i\Delta\sigma}{\omega\varepsilon_{\mathrm{vac}}} \tag{5}$$

($\varepsilon_{\mathrm{vac}}$ is the vacuum permittivity) substantially depends on the photocarrier concentration and, consequently, dramatic variation of the depolarization fields upon increase of N is also expected. It was previously shown in the frame of a simple Maxwell–Garnett effective medium model that scaling of the depolarization fields modifies the measured spectra quite differently in the percolated and non-percolated case [3].

In a number of papers a different approach is used where the spectra of macroscopic $\Delta\sigma$ are directly fit with the Drude–Smith model [6], [20]–[22]. The Drude-Smith parameters then carry information on the response of carriers as discussed in [17] or on the sample percolation. If, however, both the depolarization fields are large and the carrier response function has a non-trivial spectrum, the Drude-Smith parameters will describe both effective medium aspects and the mobility of charges at the same time; in addition, the values of these parameters will depend on N. However, up to now, no discussion has been carried out in the literature on the physical meaning of such coefficients and

the interpretation then remains on a purely phenomenological basis.

In this paper, we wish to study the dependence of experimental observables on N in a more systematic way and we propose a solution of the task (i) specified above.

In Section II, we numerically solve Maxwell equations in the quasi-static limit and we determine the scaling of the local field effect with N for various model structures (including percolated and non-percolated structures with simply curved chains of beads, fractal chains of beads and a structure containing a distribution of inclusion shapes). We show that a large class of samples showing complex percolation pathways can be described by an equivalent circuit model expressed by a simple formula depending on three parameters.

In Section III, we show in which manner our equivalent circuit model is connected to the Bergman representation of the effective medium and we provide a physical interpretation of parameters of the equivalent circuit.

In Section IV, we show that the experimental spectra depend only on the carrier response function μ and on the equivalent circuit parameters describing the effective medium effect. We propose a general formula to evaluate μ from $\Delta\sigma$.

Finally, in Section V, our findings are experimentally demonstrated on TiO_2 thin film systems prepared by sol-gel technique and by calcination of a nanoparticle network.

II. Numerical Evaluation of Depolarization Fields

In order to understand the role of depolarization fields in detail, we performed numerical simulations in 2D model structures with a constant real part ε_p and a variable imaginary part $\Delta\varepsilon''_{\rm mic}$ of the permittivity. This variable part can be understood as the transient contribution due to a photoexcitation and, taking into account the equivalence (5) between the permittivity and the conductivity, it can be identified with a real transient conductivity denoted $\Delta\sigma'_{\rm mic}$. The effective response was calculated using FreeFem++, which is a programming language and software focused on solving partial differential equations using the finite element method [23]. First, by means of a convenient image processing procedure, the 2D structures were approximated by non-uniform triangular meshes [24]. In the second step the local electric field in the sample was calculated by solving quasi-static Maxwell equations with periodic boundary conditions and with an electric field applied in a particular direction. Finally, the calculated distribution of electric energy density was averaged over the whole sample and equated to the energy density of a film with a homogeneous (effective) permittivity ε

$$\frac{1}{2}\varepsilon\langle\mathbf{E}\rangle^2 = \frac{1}{2V}\int_V \varepsilon_{\rm mic}(\mathbf{r})\mathbf{E}^2(\mathbf{r})dV. \tag{6}$$

Here $\varepsilon_{\rm mic}(\mathbf{r})$ and $\mathbf{E}(\mathbf{r})$ denote the local permittivity and the local electric field, respectively, and $\langle\mathbf{E}\rangle$ is the volume average of electric field: $\langle\mathbf{E}\rangle = V^{-1}\int_V \mathbf{E}(\mathbf{r})dV$.

In Fig. 1, we show pictures of the investigated structures. The matrix (white) has a permittivity equal to ε_m. In many works, porous semiconductor thin films are investigated and in this case the matrix is just composed of voids surrounding the nanocrystalline film; for this reason we put $\varepsilon_m = 1$ in the simulations. In the equilibrium state (step 1) the black parts possess a permittivity $\varepsilon_p = 35$ and the calculated effective permittivity is denoted as ε for each structure. In the photoexcited regime (step 2) the black parts have a permittivity $\varepsilon_p + i\Delta\varepsilon''_{\rm mic}$ and the calculation yields a macroscopic permittivity $\varepsilon + \Delta\varepsilon$, where ε is the equilibrium effective value calculated in the step 1 and $\Delta\varepsilon$ is a complex-valued change due to photoexcitation.

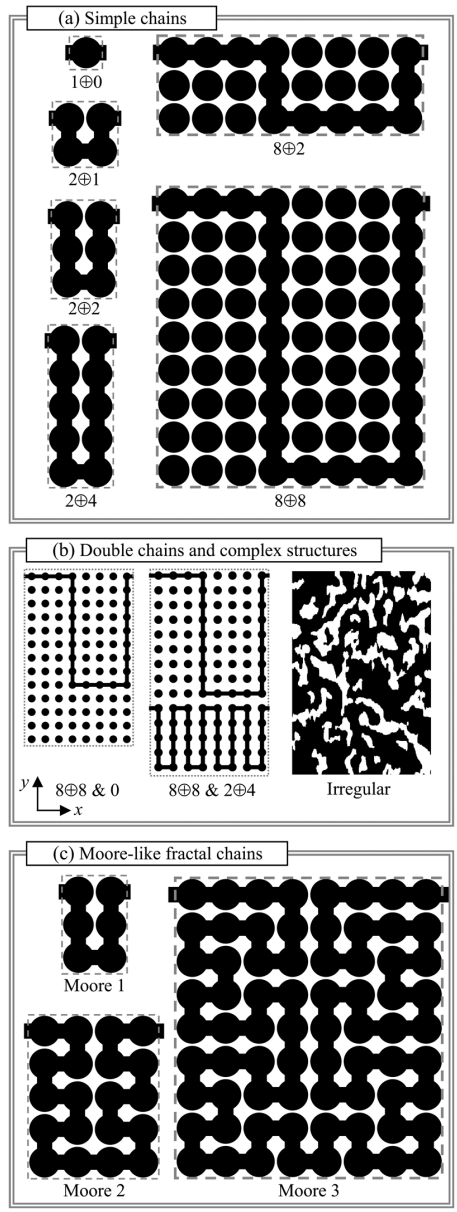

Fig. 1. Unit cells of simulated structures. Permittivity of the white part: $\varepsilon_m = 1$; permittivity of the black part: $\varepsilon_p + i\Delta\varepsilon''_{\rm mic}$, where $\varepsilon_p = 35$, $\Delta\varepsilon''_{\rm mic}$ is variable. (a) Simple chains: the numerical symbols denote here the horizontal (x) and vertical (y) extent of the percolated chain: x $\oplus$ y. (b) Double chains: only percolation pathways within the unit cell are schematically shown (beads and connectors are not in scale): in reality these structures are composed of similar arrays of connected/isolated beads as for the simple chains. Irregular structures: a structure with percolated semiconductor is shown; the inverted one (with percolated matrix) was also calculated. (c) Fractal chains: note that Moore 1 as the basic motive of fractal structures is identical to the simple chain 2 $\oplus$ 2. Besides the unit cells explicitly shown, the structures 4 $\oplus$ 1, 4 $\oplus$ 2, 8 $\oplus$ 8 & 2 $\oplus$ 1, and 8 $\oplus$ 8 & 2 $\oplus$ 2 were also studied; however, the results of simulation of these structures do not bring qualitatively new information in Fig. 2 and their fits are as good as those of the explicitly shown data.

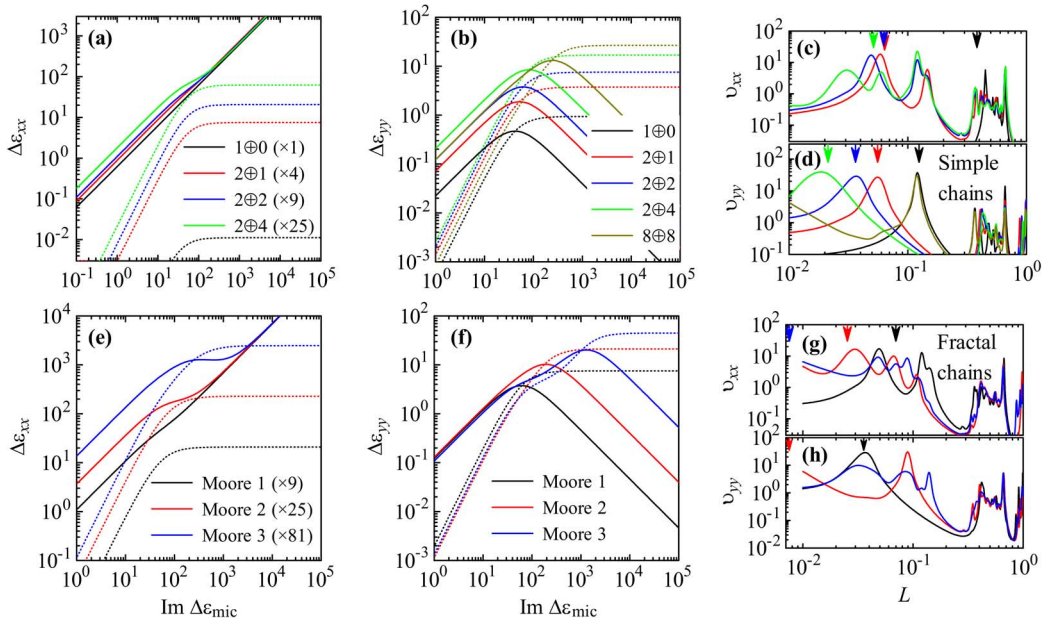

Fig. 2. (a), (b), (e), (f) Plots of the transient effective permittivity as a function of the transient microscopic permittivity obtained from finite-element calculations for selected structures from Fig. 1. Solid lines: imaginary part; dotted lines: real part. (a) percolated single chain structures (applied field//x); (b) non-percolated single chain structures (applied field//y); (e) percolated fractals (//x); (f) non-percolated fractals (//y). Plotted permittivities of percolated structures are normalized by the factor $L_x/(N \times L_y)$ which is proportional to the conductivity of the percolated chain (N is the number of connected conductive nodes within the unit cell and L_x, L_y are the horizontal and vertical sizes of the unit cell, respectively). (c), (d), (g), (h) Calculated spectral functions. Upper row: simple chains; color scheme identical to that in plots (a) and (b); Lower row: Moore-like fractal structures; color scheme identical to that in plots (e) and (f). Components for both polarizations are displayed: xx corresponds to horizontal polarization (along percolated pathway) and yy to the vertical one (non-percolated direction).

In the following we describe the relation between $\Delta\varepsilon''_{\mathrm{mic}}$ and $\Delta\varepsilon$. We can understand the scaling of $\Delta\varepsilon''_{\mathrm{mic}}$ in our model as a scaling of the photocarrier density N because, according to (1) and (5), $\Delta\varepsilon''_{\mathrm{mic}} \propto N\mu$. At the same time the variation of $\Delta\varepsilon''_{\mathrm{mic}}$ can be, in agreement with (5), associated with its frequency dependence: $\Delta\varepsilon''_{\mathrm{mic}} \propto \mu/\omega$. For the sake of clarity, in the analysis of this section we assume the microscopic mobility μ to be real and independent of ω and N; this will allows us to simplify the discussion of the dielectric behavior. For at least partly delocalized carriers ($\Delta\sigma'_{\mathrm{mic}} > 0$ in the static limit) we can state that high $\Delta\varepsilon''_{\mathrm{mic}}$ corresponds to high photoexcitation and/or low-frequency probing and low $\Delta\varepsilon''_{\mathrm{mic}}$ corresponds to a low photoexcitation and/or a high-frequency probing. However, we emphasize that the validity of our model is not limited to this assumption which is not necessarily fulfilled for the experimental data.

The results of the calculations are summarized in Fig. 2. Selected results related to simple chains are plotted in the upper row of Fig. 2 to demonstrate the trend of the response upon a change of a single percolated path in the unit cell. Structures containing two different percolation paths in the unit cell (double chains) were studied in order to estimate the role of combination of different chains on the effective conductive response. However, results concerning these structures do not exhibit any qualitatively new features compared to single chains and therefore they are not plotted in Fig. 2. Fractal chains represent a series of structures with increasing complexity and chain length—their response is shown in the lower row of Fig. 2. All these "mathematically ordered" structures were compared with percolated and non-percolated highly disordered structures (irregular structure in Fig. 1) to strengthen our arguments for a general impact of the results. Again we found that these irregular structures do not bring any qualitatively new feature to the effective response compared to simple chains.

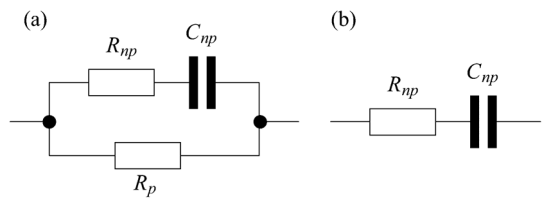

Fig. 3. Equivalent electrical circuits describing the effective response of the simulated structures shown and described in Fig. 1; (a) percolated and (b) non-percolated samples.

The behavior can be understood in terms of an equivalent electrical circuit shown in Fig. 3. The admittance (representing the effective transient conductivity of the sample) reads:

$$Y = \frac{1}{R_p} + \frac{\frac{1}{R_{np}}}{1 + i/(\omega C_{np} R_{np})}. \tag{7}$$

This formula describes well the observed change of the regime of the effective conductivity in the middle of the studied range of $\Delta\varepsilon''_{\mathrm{mic}}$.

In a percolated structure [electric field applied along x in Fig. 1; Fig. 2(a), (e)], a continuous more or less complex path exists across the structure and it is taken into account by the parallel resistance R_p (inversely proportional to $\Delta\varepsilon''_{\mathrm{mic}}$ for each structure). If this part of the circuit dominates ($R_p \to 0$) the effective transient conductivity of the sample is directly proportional to the microscopic transient conductivity of particles

$\Delta\sigma'_{\rm mic}$. Also the percolated part of the circuit yields a non-zero dc conductivity if $\Delta\sigma'_{\rm mic}(\omega = 0) > 0$.

A capacitive coupling between some parts of the percolated path and between non-percolated inclusions may also contribute. This is taken into account by the $R_{np} - C_{np}$ branch in Fig. 3, which contributes particularly when R_p becomes high ($\Delta\varepsilon''_{\rm mic}$ becomes low). Again, $1/R_{np}$ is proportional to $\Delta\varepsilon''_{\rm mic}$ while C_{np} is constant and depends essentially on the pathway geometry and matrix permittivity. Since the effective capacitance of the sample is limited by the capacitance of the non-conducting matrix, $\Delta\varepsilon'$ shows a saturated behavior for high $\Delta\varepsilon''_{\rm mic}$ (i.e., for high photoexcitation or for low frequencies). The position of the elbow clearly observed in Fig. 2(a), (e), which marks a change of the effective conductivity regime, then essentially depends on the magnitude of C_{np}. The capacitance role can be illustrated by a comparison of Fig. 2(a) and (e). Geometries with dense narrow bridges between distant parts of the percolated path such as fractal structures exhibit a higher capacitance; consequently, the change of the conductivity regime occurs at clearly higher values of $\Delta\varepsilon''_{\rm mic}$ (i.e., at higher local conductivity and lower frequencies).

Non-percolated structures do not show any continuous conducting path and the resistance R_p is thus missing in the equivalent circuit ($R_p \to \infty$). For this reason, there is no real conduction for high $\Delta\varepsilon''_{\rm mic}$ ($\Delta\sigma'_{\rm mic}$) which implies that $\Delta\varepsilon''$ decreases towards zero for growing $\Delta\varepsilon''_{\rm mic}$. For low $\Delta\varepsilon''_{\rm mic}$ (low photoexcitation and/or high frequencies) the capacitive reactance is negligible compared to the real conductance and the effective transient conductivity is thus directly proportional to $\Delta\varepsilon''_{\rm mic}$ similarly as in percolated structures.

III. Analysis Within the Spectral Function Representation

The equivalent circuit model can be further discussed within the framework of an analysis based on the Bergman spectral representation [25]. For a two-component system in equilibrium, the effective permittivity may be written as follows [26]:

$$\varepsilon = V_m\varepsilon_m + V_p\varepsilon_p + \int_0^1 \frac{v(L)\varepsilon_m\varepsilon_p}{(1-L)\varepsilon_p + L\varepsilon_m}dL \qquad (8)$$

where V_m and V_p are the percolation strengths of ε_m and ε_p components in the direction of the probing field, respectively; the integral represents the contribution of non-percolated clusters characterized by the depolarization factor L and weighted by the spectral function $v(L)$. In the language of our previous analysis the integral in (8) can be regarded as a parallel connection of infinite number of $R_{np} - C_{np}$ branches with some specific properties and the weight V_p of the percolated part is connected to the parallel resistance R_p. We found in the previous section that a single $R_{np} - C_{np}$ branch is sufficient to describe the effect of depolarization fields. This leads us to an assumption that the spectral function can be approximated by a dominant peak for a single depolarization factor L_j and we can simply write $v(L) = v_j\delta(L - L_j)$. The transient effective permittivity $\Delta\varepsilon$ is then defined as the difference between the effective permittivities with and without photoexcitation:

$$\Delta\varepsilon = V_m\varepsilon_m + V_p(\varepsilon_p + \Delta\varepsilon_{\rm mic}) + \frac{v_j\varepsilon_m(\varepsilon_p + \Delta\varepsilon_{\rm mic})}{(1-L_j)(\varepsilon_p + \Delta\varepsilon_{\rm mic}) + L_j\varepsilon_m} - \varepsilon \qquad (9)$$

which yields

$$\Delta\varepsilon = \Delta\varepsilon_{\rm mic}\left[V_p + \frac{B_j}{1 + D_j\Delta\varepsilon_{\rm mic}}\right] \qquad (10)$$

where we have introduced:

$$B_j = \frac{L_j\varepsilon_m^2 v_j}{\left[(1-L_j)\varepsilon_p + L_j\varepsilon_m\right]^2} \qquad (11)$$

$$D_j = \frac{1-L_j}{(1-L_j)\varepsilon_p + L_j\varepsilon_m}. \qquad (12)$$

In terms of the conductivity, taking into account (5), the expression (10) reads

$$\Delta\sigma = \Delta\sigma_{\rm mic}V_j + \frac{\Delta\sigma_{\rm mic}B_j}{1 + iD_j\Delta\sigma_{\rm mic}/\omega\varepsilon_{\rm vac}}, \qquad (13)$$

which exactly corresponds to the admittance of the equivalent circuit given by (7).

We fitted the calculated dependences $\Delta\varepsilon$ on $\Delta\varepsilon''_{\rm mic}$ for all the structures studied with the model (10) that was shown to be equivalent to the circuit introduced in Fig. 3 and described by (7). The fit yields coefficients V_p, B_j and D_j which are *a priori* unknown for a given structure. Fig. 4 shows the residuals of these fits and their behavior allows us to conclude that in the majority of cases our simple model reproduces well the numerically calculated data. The residuals start to increase more substantially only for highly complex percolation pathways such as the fractal structures from Fig. 1. This behavior is, however, expected to a large extent: there are high capacitances between parts of chains with a broad distribution of lengths and positions. In other words, there are several branches $R_{np} - C_{np}$ with a broad distribution of properties (i.e. several different depolarization factors come into play). It can be also seen in Fig. 4 that in the case of fractal structures a better match is obtained for the percolated structures, where a significant part of the response is captured by the more directly accessible coefficient V_p, than for non-percolated ones.

An important point concerns a possible physical interpretation of the coefficients V_p, B_j and D_j which characterize the equivalent circuit of the effective medium approximation. The coefficient V_p directly describes the contribution of the percolated part to the effective conductivity whereas the meaning of the coefficients B_j and D_j (related to the $R_{np} - C_{np}$ branch) is less straightforward. In our analysis we approximated a possibly complex spectral function by a single delta-peak at the position L_j:

$$L_j = \left[1 + D_j\varepsilon_m/(1 - D_j\varepsilon_p)\right]^{-1}. \qquad (14)$$

A question now arises whether the position of this peak, as determined from the experiment by means of the parameter D_j, may reveal some important properties of the sample nanostructure.

To investigate this, we reconstructed the spectral function of each model structure by using a calculation described in Appendix A. In Fig. 2(c), (d), (g), (h) the positions of the main peaks of the spectral function are compared to the values L_j evaluated from the parameter D_j with the help of (14). We observe that the calculated depolarization factors L_j reasonably agree with the position of the first peak in the spectral function

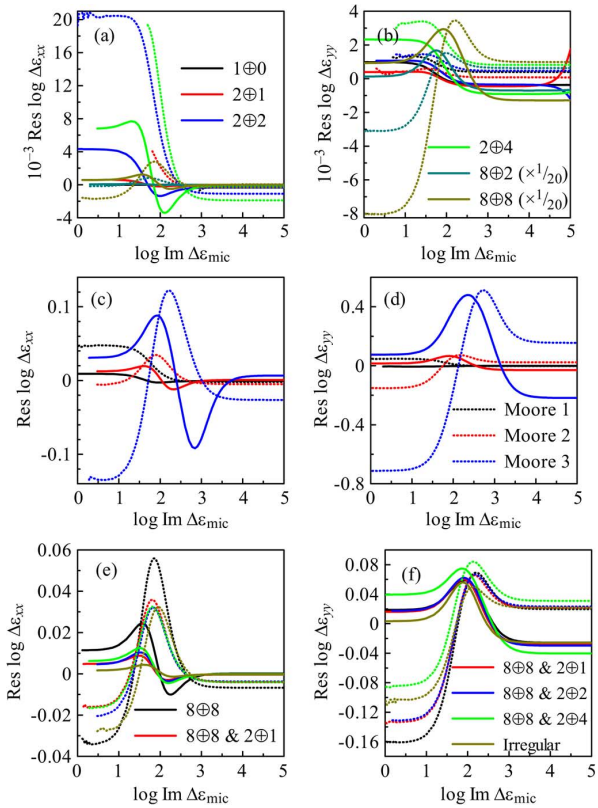

Fig. 4. Residuals of the fits of log $\Delta\varepsilon$ by (10). Upper row: simple chains; middle row: Moore-like fractal structures, lower row: Double chains and complex structures. Dotted lines: real part; solid lines: imaginary part. Components for both polarizations are displayed: xx corresponds to horizontal polarization (along percolated pathway) and yy to the vertical one (non-percolated direction), see Fig. 1.

(i.e. of the peak with the smallest L_j), but not necessarily with the biggest one. This can be explained as follows. We observe that the dependence $\Delta\varepsilon(\Delta\varepsilon''_{\rm mic})$ mainly reflects the conducting properties of the structure if there are any. It means that $\Delta\varepsilon$ is sensitive to the existence of direct percolation paths (formally $L = 0$) and to the response of structures with low L_j which are essentially continuous features with narrow interruptions. In contrast, large depolarization factors determine mainly the capacitive response which can be hardly retrieved in our model with a single RC resonance and for its description it would be necessary to introduce additional parallel RC terms. In this context it should be stressed that these higher resonances observed in the plots of the spectral function in Fig. 2(c), (d), (g), (h) contribute only little to the permittivity and this contribution can be hardly detected in the case of positive ε_p.

The determination of the coefficients D_j and of the dominant depolarization factor L_j from the experimental data then seems to have a good physical sense if the spectral function contains a single peak with low L_j substantially higher than any features close to $L = 0$.

We discussed in detail the macroscopic response of the inhomogeneous sample upon photoexcitation where $\Delta\varepsilon_{\rm mic}$ is purely imaginary. Let us stress, however, that our model based on (13) is also valid for a complex-valued transient permittivity $\Delta\varepsilon_{\rm mic}$ (i.e. with a finite real part). Indeed, in our analysis we consider a dielectric or semiconductor material with a positive equilibrium ε_p and poles in the argument of the integral in (8) do exist only for a negative ε_p. The photoexcitation thus cannot bring the total permittivity $\varepsilon_p + \Delta\varepsilon_{\rm mic}$ significantly closer to the poles. In this regime, no qualitatively new behavior is expected in comparison with the effective macroscopic responses shown in Fig. 2(a), (b), (e), (f). In this sense, considering that $\Delta\sigma_{\rm mic}$ in (13) can be complex, the resistances R_p and R_{np} in formula (7) and in the equivalent circuits depicted in Fig. 3 can be understood as impedances Z_p and Z_{np} of the percolated and non-percolated parts. Their possible frequency dispersion is then related to the microscopic transport mechanisms defined by the dispersion of $\Delta\sigma_{\rm mic}$.

Equation (13) explicitly dismantles the problem into two parts specified in the introduction. Task (i) related to the description of depolarization fields is reduced to determination of coefficients V_p, B_j, and D_j and task (ii) aiming the understanding of the nanoscopic charge transport consists in the modeling of the microscopic conductivity $\Delta\sigma_{\rm mic}$.

Finally, let us note that Maxwell–Garnett effective medium model is a special case of the Bergman representation with a single peak in the spectral function occurring at the depolarization factor value $L = (1 - s)/3$ for spherical inclusions [27], where s is their filling factor (in the case of higher filling factor it is known as Hashin-Shtrikman model). It can be easily shown that the Maxwell–Garnett model can describe two types of structures: non-percolated photoconducting inclusions in a percolated insulating matrix, and inversely, non-percolated insulating matrix voids in percolated photoconducting clusters of inclusions. The corresponding mathematical expressions are equivalent to (13)—cf. (13) and (14) in [3]. Comparison of these equations also permits determining the coefficients V_p, B_j, and D_j in the Maxwell–Garnett approximation. However, let us point out that this model cannot describe structures, in which both materials are percolated.

IV. Role of the Effective Medium in Pump–Probe Experiments

Up to now, we have shown that for many geometrical layouts of percolated and non-percolated photoconductive samples, the effect of depolarization fields can be expressed by a simple model (10) with 3 real parameters V_p, B_j and D_j. The aim of this paragraph is to show the way how to apply our model to experimental data. To achieve this we need to estimate the role of microscopic parameters in the macroscopic response and the role of inhomogeneous distribution of carriers in the sample.

In real samples there may be several types of inclusions with different size, structure or phase (e.g. amorphous vs. crystalline); even if these types of inclusions (from now on denoted by index j) possess the same or very similar equilibrium permittivity value ε_p, each one may need to be characterized by a different photoconductivity mechanism (i.e. different yield-mobility product spectrum denoted by $\xi_j\mu_j$).

Then we need to distinguish between the percolation strengths corresponding to these individual components:

$$V_p = \sum_j V_j \tag{15}$$

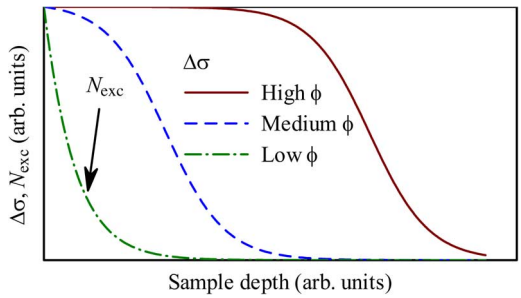

Fig. 5. Illustration of the depth profile of effective $\Delta\sigma$ when the pump photon density ϕ (and, consequently, excitation density $N_{\rm exc}$ and microscopic conductivity $\Delta\sigma_{\rm mic}$) are scaled. At low photoexcitation level $\Delta\sigma$ follows the exponential absorption law ($\Delta\sigma \propto \Delta\sigma_{\rm mic}$); at medium and high pump a saturation of close to the irradiated surface occurs following (13).

Also the spectral function $v(L)$ is then approximated by a sum of a few delta functions

$$v(L) = \sum_j v_j \delta(L - L_j) \tag{16}$$

and we obtain

$$\Delta\varepsilon = \sum_j \Delta\varepsilon_j \left[V_j + \frac{B_j}{1 + D_j \Delta\varepsilon_j} \right] \tag{17}$$

where B_j and D_j were defined by (11) and (12), respectively, and $\Delta\varepsilon_j$ are transient microscopic permittivities of the individual components. Equations (10) and (17) have an important practical impact. We expect that this is a good phenomenological approximation describing the effect of depolarization fields in many structures encountered in real samples.

To interpret the experimental data, it is usually assumed that the transient conductivity of photoexcited samples decreases exponentially with depth; this condition naturally arises from the exponential Lambert–Beer absorption law for the pump beam. Note that, for example, (3) was derived under this assumption [12]. However, as it was also pointed out previously [3], the effect of strong depolarization fields leads to a nonlinear behavior of the effective permittivity or conductivity in the non-percolated case. The nonlinear character of (17) in $\Delta\varepsilon_j$ or of (13) in $\Delta\sigma_{\rm mic}$ is clearly seen. This nonlinearity causes a deviation of the depth dependence of the effective conductivity from the exponential law for complex sample morphologies. In particular, for high excitation densities the effective conductivity or permittivity corresponding to the non-percolated part in (17) may saturate close to the irradiated surface despite the fact that some of $\Delta\varepsilon_j$ grow with the absorbed pump fluence. This is because the term $D_j\Delta\varepsilon_j$ will dominate in the denominator of (17). In contrast, at low photoexcitation level $\Delta\varepsilon$ will be proportional to $\Delta\varepsilon_j$. This behavior is illustrated in Fig. 5.

For this reason, we derive an expression accounting for this behavior. We start from [12, eq. (30)]—cf. also with (3)—which is valid for an infinitesimally thin photoexcited layer. The total transient transmittance then reads

$$\frac{\Delta E}{E} = -\frac{z_0}{n_1 + n_2} \int_0^d \Delta\sigma(z) dz \tag{18}$$

where d is the thickness of the thin film sample and where $\Delta\sigma(z)$ is calculated from $\Delta\varepsilon(z)$ given by (17) with $\Delta\varepsilon_j(z) = \Delta\varepsilon_{0j}\exp(-\alpha z)$; α is an effective absorption coefficient of the excitation beam in the composite sample. It is assumed that all the pump power is absorbed in the sample, i.e., $\exp(-\alpha d) \to 0$. We express the result of the integration in (18) in a convenient form as the normalized transient sheet conductivity [cf. with (3), (4)]

$$\begin{aligned} -\frac{(n_1 + n_2)}{z_0} \frac{1}{e\phi} \frac{\Delta E}{E} &\equiv \Delta X_\sigma \\ &= \sum_j \frac{\alpha_j}{\alpha} \left[\xi_j \mu_j V_j + B_j \frac{\ln(1 + i\xi_j \mu_j D_j u_j)}{i D_j u_j} \right] \end{aligned} \tag{19}$$

where α_j is the optical absorption coefficient in the jth component and

$$u_j = \frac{e\phi\alpha_j}{\omega\varepsilon_{\rm vac}}. \tag{20}$$

Equation (19) is the crucial result of our theoretical analysis. It relates the directly measurable transient transmission at the left-hand side with the microscopic transport response functions (yield-mobility products of photoconductive components) and with the coefficients V_j, D_j, B_j related to the equivalent circuit in Fig. 3(a) accounting for the effective medium effect.

Note that (19) approaches the form of (3) in two cases: (a) the contribution of the non-percolated part is negligible ($B_j \to 0$) or (b) the local photoinduced permittivity is low ($\xi_j\mu_j D_j u_j \to 0$). In the latter case the second term in square brackets in (19) also becomes simply proportional to $\xi_j\mu_j$. In both these cases the normalized sheet conductivity will not depend any more on N.

Note also, that unlike (3), (19) requires the knowledge of the absorption coefficients (of individual components and of the sample as a whole) and it essentially depends on the morphology of the system.

V. Experimental Results

Macroporous titania thin films were fabricated by a co-assembly of different titania precursors and polymethylmethacrylate (PMMA) beads with the size of ~320 nm used as templates for the porosity. Three types of titania films deposited by spin coating and assembled from titania precursor with different crystallinity were investigated experimentally. The films denoted as *np* were assembled from crystalline TiO_2 nanoparticles with the size of ~20 nm (*np* precursor), the films denoted as *sg* were assembled from the sol-gel derived amorphous titania (*sg* precursor), and the films denoted *sg-np* were prepared by a "brick and mortar" approach from *np* and *sg* precursors (*np-sg* precursor). A more detailed description of the precursor solutions preparation is provided in Appendix B. Dried films were heated in air for 1 hour at 400 °C (achieved with a slow heating ramp of 1 °C/min) to remove the PMMA template, resulting, after calcination, in macroporous thin semitransparent titania films which slightly scatter the visible light. The average thickness of the films is about 1 μm.

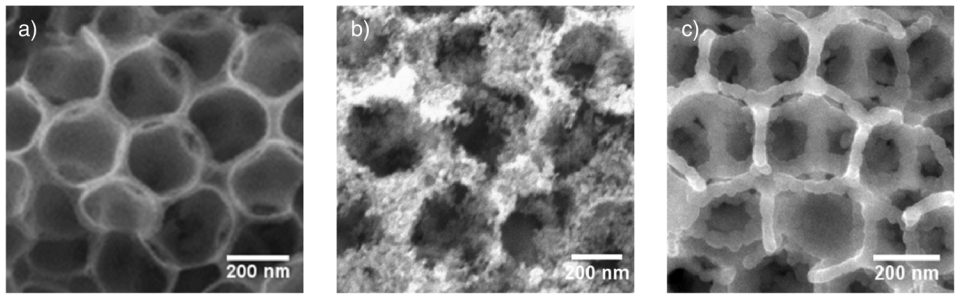

Fig. 6. SEM images (top view) of the macroporous titania films after calcination at 400 °C obtained by a co-assembly of PMMA beads and (a) sol-gel derived titania sg, (b) crystalline titania nanoparticles np and (c) "brick and mortar" mixture of sg-np precursors.

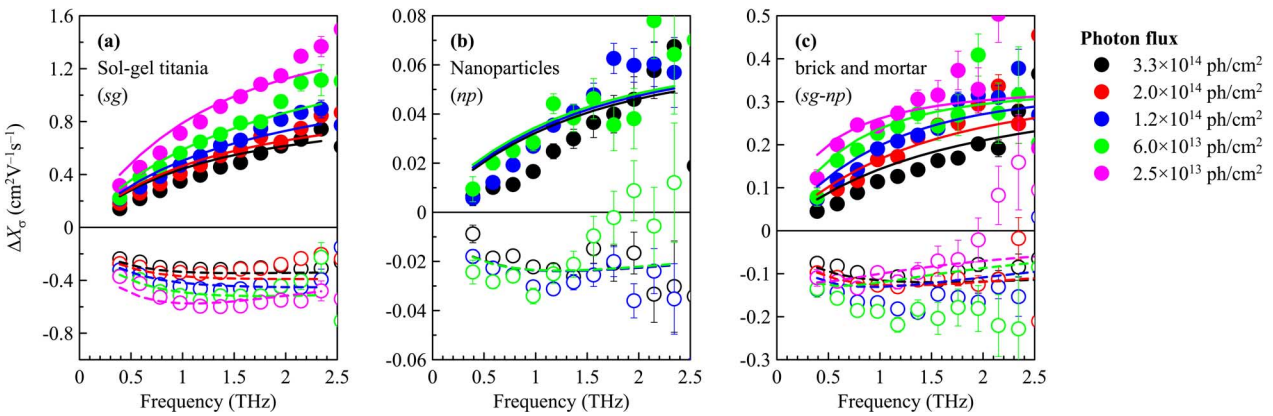

Fig. 7. Spectra of the normalized transient sheet conductivity vs. pump photon density for the pump-probe delay of 10 ps for 3 samples studied. Symbols: experiment, lines: fits with (22). Error bars correspond to the standard deviation of a statistical ensemble of data.

Films obtained from all precursors have an open macroporous morphology with a uniform pore size of ∼250 nm but rather low periodicity of the pore ordering (Fig. 6). The resulting titania scaffold is actually a negative replica of the cubic close packed PMMA spheres. All the titania films obtained after calcination at 400 °C are crystalline corresponding to the anatase phase. An average size of the crystalline domains in all the samples is 20 ± 4 nm as estimated from the XRD peak broadening. Although the crystallite size in the titania films obtained from different precursors is similar, their connectivity in the titania scaffold is different. As it can be seen from the SEM images in Fig. 6, the walls of the sg and np-sg titania scaffolds are compact, while the walls of the np sample are formed by loosely packed crystalline nanoparticles.

Transient THz conductivity spectra were measured in a usual setup for time-resolved THz spectroscopy [4] driven by a Ti:sapphire laser amplifier (Spitfire ACE, central wavelength 800 nm, 1 mJ pulse energy, 5 kHz repetition rate). A part of the laser beam was frequency tripled and the resulting wavelength of 266 nm (4.66 eV) was used to generate conduction-band charges in the investigated samples. The pump beam was defocused in order to produce a homogeneous excitation of the probed part of the sample: 15% of the pump power passed through an empty 3 mm aperture which was attached to the back face of the sample during the pump-probe experiments. The penetration depth of the radiation at 266 nm in a bulk TiO_2 is ∼20 nm. It means that the highest excitation flux of 3.3×10^{14} photons/cm^2 used in our experiments would produce an excitation density of $N_{\mathrm{exc}} = 1.6 \times 10^{20}$ cm^{-3} in bulk TiO_2. The pump beam intensity incident on the sample was varied by means of beamsplitters with a variable transmittance for 266 nm. The accumulation of THz transient transmission spectra for the lowest pump fluences took up to 24 hours.

In Fig. 7, we show the normalized transient sheet conductivity X_σ (19) for THz probing 10 ps after photoexcitation. One clearly observes a marked dependence of this signal on the pump photon fluence in the sg and sg-np samples whereas only a minor evolution of the spectral shape is seen in the np sample. In the following considerations, we will neglect a possible dependence of the microscopic mobility on the excitation density, as in other works on TiO_2 nanocrystals it was shown to be negligible in the range of the used excitation intensities [28], [29]. This is to say that we assume the observed dependence of the normalized transient sheet conductivity on the excitation density to be entirely governed by depolarization fields in the samples. We examined two simple models, which differ by the mechanisms of the microscopic mobility. The starting point of our analysis is (19) as the main result of our effective medium theory where the model behavior of the mobility μ_j is injected.

1) At the first sight, a suitable model consists in the assumption that microscopic charge mobility is controlled by localization-modified Drude model calculated by Monte Carlo simulations [17]. In order to make fitting of the data easier in our first approach, we approximated the microscopic mobility behavior by the Drude–Smith model similarly as it was shown in [17]. In such a case, we obtained very good fits of the measured data with the following Drude–Smith parameters: Drude–Smith scattering

time $\tau_{\rm DS}$ reaching 60–80 fs, and the backscattering coefficient c_1 close to -1. However, the Drude–Smith scattering time is unrealistically long. In [17] it was shown that $\tau_{\rm DS}$ must be shorter than the bulk momentum relaxation time; our results then would imply bulk mobilities exceeding 100 $\rm cm^2 \cdot V^{-1} \cdot s^{-1}$. This value has to be compared with the dc mobility in a good-quality anatase crystal ($20 \rm cm^2 \cdot V^{-1} \cdot s^{-1}$ [30]) and with the THz mobility in anatase micro- and nanoparticles ($3.6 \rm cm^2 \cdot V^{-1} \cdot s^{-1}$ [29]). In addition, the observed amplitudes of the normalized transient signal are very low. This would require a very low quantum yield of free charges (e.g., 1.4% in the sg sample and 0.1% in the np sample) or a quite small value of α_j/α, where α_j is the absorption coefficient in bulk anatase and α is the absorption coefficient of the sample as a whole (including defects, voids, and organic rests). Although there may be strong absorption on defect states or on rests of the organic vehicle, such small yields would imply that anatase forms a minority phase in the samples. Based on these considerations the model does not seem to be plausible.

2) In the second model, we considered that microscopic mobility is governed by two conduction mechanisms: hopping (described by the Dyre random free-energy barrier model, [31]), and band-like conduction (with the Drude behavior). The fits converged to the situation where the band-like conduction (denoted by index D) takes place in non-percolated parts, i.e. it is described by the second term at the right hand side of (19). Concerning the hopping conduction (denoted by index h), its contribution was found to be linear, i.e., $\Delta X_{\sigma,\rm h} \propto \mu_{\rm h}$ in terms of (19). This means that the hopping should occur along the percolated pathways and/or the logarithmic term describing the contribution from non-percolated parts is reduced to a linear one. As discussed above, this last contribution may occur when the local photoinduced permittivity is quite low ($\xi_{\rm h}\mu_{\rm h}D_{\rm h}u_{\rm h} \to 0$). We will come back to this discussion after the presentation of the fit parameters: their values will allow us to estimate the weight of these two contributions. We start our analysis with a simplified formula (19):

$$\Delta X_\sigma = \frac{\alpha_{\rm h}}{\alpha}\xi_{\rm h}\mu_{\rm h}(V_{\rm h}+B_{\rm h}) + B_{\rm D}\frac{\alpha_{\rm D}}{\alpha}\frac{\ln(1+i\xi_{\rm D}\mu_{\rm D}D_{\rm D}u_{\rm D})}{iD_{\rm D}u_{\rm D}}. \tag{21}$$

Only some of the parameters in (21) can be determined independently from the experiment. Taking into account the expression (20), the frequency dependence of $\mu_{\rm h}$—see [32, eq. (1)]—and that of $\mu_{\rm D}$, we rewrite formula (21) in the following form which was used for the fitting of the experimental data:

$$\Delta X_\sigma = A\mu_{\rm h}(\omega;\tau_{\min},\tau_{\max}) - i\omega\frac{\varepsilon_{\rm vac}}{eN_{\rm exc}}\frac{\beta}{\delta}\ln\left[1-\frac{eN_{\rm exc}}{\varepsilon_{\rm vac}}\frac{\delta}{(i\omega+\omega^2\tau_{\rm D})}\right]. \tag{22}$$

The relevant fitting parameters are described in Table I. The time $\tau_{\max}$ represents the longest waiting time found in the system; it is well below the THz range and cannot be determined from our fits. The Drude momentum relaxation time $\tau_{\rm D}$ was fixed to 1 fs: the spectrum of $\mu_{\rm D}$ is then flat and its imaginary part is negligible compared to the real part. A variation of the value of $\tau_{\rm D}$ up to ~20 fs does not change significantly the shape of the spectral response and it leads merely to an amplitude scaling of the Drude microscopic mobility (up to $e\tau_{\rm D}/m_e \sim 35$ $\rm cm^2 \cdot V^{-1} \cdot s^{-1}$); this ensures that our fit is compatible with the dc mobility of anatase. The maximum hopping frequency $1/\tau_{\min}$ is of the order of phonon frequency [33], in agreement with the assumptions of the hopping model [31].

TABLE I
SUMMARY OF EXPERIMENTAL RESULTS IN THIN FILM TiO_2 SAMPLES

TiO_2	sol-gel (*sg*)	nanoparticles (*np*)	brick and mortar (*sg-np*)
$\tau_{\min}$ [fs]	80	58	84
A [$\rm cm^2V^{-1}s^{-1}$]	0.66	0.059	0.15
$\tau_{\rm D}$ [fs]	1 (fixed)	1 (fixed)	1 (fixed)
β [$\rm cm^2V^{-1}s^{-1}$]	0.81	0	0.18
δ [$\rm cm^2V^{-1}s^{-1}$]	0.73	—	0.11

Note that the model contains only four free parameters to fit a set of ~10 spectra for each sample. For both very high and very low pump fluences the normalized transient sheet conductivity (22) does not depend on $N_{\rm exc}$; in the high excitation limit ΔX_σ is merely due to the hopping contribution while in the low excitation limit ΔX_σ is given by a sum of the hopping and a simple Drude term. For the highest pump fluence we used, the amplitude of the spectra is accounted for by A while their shape is set mainly by $\tau_{\min}$. The parameter δ determines the characteristic value of excitation density $N_{\rm exc}$ above which the shape of the spectrum starts to change (the contribution of the Drude term starts to diminish), whereas the parameter β describes the strength of this change. There is no free parameter controlling the change of the spectral shape with excitation fluence; this dependence stems directly from the application of the effective medium approximation.

The results can be understood as follows. The conduction in bare nanoparticles (np) is dominated by the hopping mechanism. On the one hand, this result is intriguing in the light of observation of band-like transport in TiO_2 nanoparticles prepared in various ways [9], [28], [34], [35]. On the other hand, experiments in Nb-doped TiO_2 nanoparticles showed that the hopping conduction mechanism can have an important role in these systems as well [32]. Comparison of all these results indicates that the mobility level and the underlying conduction mechanism of microscopic mobility are dramatically dependent on the method of nanoparticles fabrication. Our results suggest that the nanoparticles under study exhibit a very low mobility of electrons compared to the above references.

In order to analyze the hopping transport more in detail, we estimate the parameter $D_{\rm h} \sim (2-3)\times 10^{-2}$ for reasonable values of $L_{\rm h}(\leq 0.9)$. Under these conditions the term $\xi_{\rm h}\mu_{\rm h}D_{\rm h}u_{\rm h}$ is substantially smaller than 1 for $\xi_{\rm h}\mu_{\rm h} < 0.3$ $\rm cm^2 \cdot V^{-1} \cdot s^{-1}$. Taking into account these estimations we finally find that the contribution of the non-percolated parts to the effective hopping conductivity $\xi_{\rm h}\mu_{\rm h}B_{\rm h}$ in (21) must be much smaller than 0.01 $\rm cm^2 \cdot V^{-1} \cdot s^{-1}$ (one can estimate that $B_{\rm h} \leq 0.04$ for $L_{\rm h} \leq 0.9$) which is quite negligible with respect to the values of the parameter A in Table I. We conclude that hopping occurs along the percolated paths in all the samples.

The contribution of hopping in sg titania in the percolated phase is about an order of magnitude higher than that in np sample. In addition, we observe that the measured normalized transient sheet conductivity is pump intensity dependent which suggests a non-negligible Drude-like conduction in the non-percolated phase. It is possible that the sol-gel derived titania network contains on one side closely packed nanocrystals in which the hopping dominates and, besides that, a very small amount of "better quality" crystalline titania phase with band-like conduction. The mobility in such clusters could be several orders of magnitude higher than that of the hopping conductivity; this implies that even a very small amount of such clusters may lead to a signal comparable with the hopping contribution which has a very small mobility. The fits of the experimental data provide very similar values of β and δ for the Drude-like contribution (Table I). It means that the coefficients B_{D} and D_{D} of (21) should acquire similar values. This condition is met approximately for $L_{\mathrm{D}} \approx 0.8$–$0.9$. We have recently observed a very similar two-component behavior in a system of nanocrystalline silicon where some sparse larger Si grains with high band-like mobility are also observed [36].

Finally, the properties of sg-np sample lie somewhere between the properties of the sg and np samples. The hopping frequency is very close to that found in sg sample, which corroborates the view that the porous titania phase still dominates the conductivity. We observe that the hopping amplitude decreases by a factor of 4, which is not surprising if we take into account the fact that a relatively well conducting sol-gel derived titania network is now completed by poorly conducting nanoparticles. The presence of the Drude component shows that the large crystalline phase found in sg sample does exist also in sg-np sample.

VI. Conclusion

Retrieval of local photoconductive properties of nanostructured and disordered semiconductors is a tricky task due to the inherently inhomogeneous nature of samples. The effective photoinduced conductivity measured in time-resolved THz experiments features a medley of two effects: effect of depolarization fields and that of the charge carrier transport on the nanoscale. In this paper we proposed a way to extract both of them quasi-independently without *ad hoc* assumptions about the sample nanostructure and percolation state and without further excessive numerical modeling for each particular sample.

We performed extensive numerical simulations of the local field distribution in a large number of model structures; the results allowed us to set up an effective medium model able to describe a macroscopic response of a broad class of percolated and non-percolated structures by means of three parameters accessible experimentally. To benefit from this analysis the THz experiments must be carried out as a function of the excitation density (optical pump pulse fluence). The normalized transient transmission function (19) depending on the frequency and on the excitation density is then expressed as a function of the microscopic mobility μ of carriers and three effective-medium parameters. Our method is demonstrated on a series of TiO_2 thin films: the local transport mechanisms were successfully uncovered for these samples.

Appendix A
Reconstruction of Spectral Function

The reconstruction of the spectral function of each model structure was performed with the help of the numerical calculations described in Section II. The argument of the integral in (8) exhibits a pole at some $L = L_0$ for any negative value of ε_p. This pole corresponds to a localized plasmon resonance and $v(L_0)$ constitutes a dominant contribution to the effective permittivity. We formally substitute

$$\left(\frac{\varepsilon_m}{\varepsilon_p} - 1\right)^{-1} = -(L_0 + is) \tag{23}$$

into (8) (s is a very small positive number); it follows [37] that we can retrieve the spectral function at any value L_0:

$$v(L_0) = -\frac{1}{\pi L_0} \lim_{s \to 0} \left[\mathrm{Im} \frac{\varepsilon(L_0 + is)}{\varepsilon_m}\right] \tag{24}$$

where ε is the numerically calculated effective permittivity of the structure for the appropriate negative ε_p. In other words, to retrieve the spectral function for a specific depolarization factor L_0, we must calculate ε for negative ε_p given by (23). In this way the spectral functions were calculated for all the structures ($s = 0.005$ in our numerical calculations) and the results are shown in Fig. 2(c), (d), (g), (h). We point out that a detailed discussion based on this formalism has been already carried out in the literature ([38] and references therein) aiming at a retrieval of the spectral function from the experimental data obtained in a reststrahlung band of the material where ε_p reaches negative values.

Appendix B
Sample Preparation

PMMA Nanoparticles: The nanoparticles with the size of ~320 nm were synthesized via an emulsion polymerization route described elsewhere [39]. In brief, potassium peroxodisulfate $K_2S_2O_8$ (56 mg) in 2 mL water was injected in a mixture of sodium dodecylsulfate (5.6 mg) and methylmethacrylate (35.5 g) in 98.0 mL water to initiate polymerization. The reaction mixture was stirred for 2 h at 90 °C, then exposed to air and cooled with an ice bath. The colloidal solution was stirred over night, filtered over glass wool, washed three times by centrifugation and redispersion in water and dried to obtain PMMA powder.

np Precursor Solution: Crystalline anatase nanoparticles were prepared according to a procedure described elsewhere [40]. In brief, a mixture of 9.47 g titanium isopropoxide and 1.90 ml acetic acid (conc.) was hydrolyzed by 48.5 ml water to form a white precipitate; afterwards 4 ml of nitric acid (conc.) was added and the mixture was refluxed for 75 min. After addition of 0.44 ml of water the mixture was transferred to a PTFE-lined autoclave and left at 250 °C for 12 hours. The reacted mixture containing a white precipitate was ultrasonicated for 1 hour after addition of 0.40 ml of 65% nitric acid and then concentrated by a rotary evaporation. The titania nanoparticles were washed three times with absolute EtOH by repetitive redispersion and centrifugation. For the preparation of the solutions for spin-coating, 325 mg of dried PMMA nanoparticle was added to a dispersion of 100 mg of the titania nanoparticles in 4 mL absolute ethanol and the solution was stirred overnight.

sg Precursor Solution: PMMA nanoparticles (325 mg) were well dispersed in 4 mL ethanol by ultrasonication for several hours, then tetraethylorthotitanate (TEOT, 0.36 g) was added and the mixture was stirred for another hour at room temperature. Finally, 230 μL of 37% HCl was added and the solution was freshly used for spin-coating without any additional aging.

sg-np Precursor Solution: A mixture of np titania nanoparticles (70 mg) and PMMA nanoparticles (325 mg) in 4 mL ethanol was stirred overnight, afterwards 108 mg of TEOT was added and the mixture was stirred for 1 h at room temperature. Finally, 69 μL HCl (37%) was added to obtain the final mixture for spin-coating.

REFERENCES

[1] R. Ulbricht, E. Hendry, J. Shan, T. F. Heinz, and M. Bonn, "Carrier dynamics in semiconductors studied with time-resolved terahertz spectroscopy," *Rev. Mod. Phys.*, vol. 83, p. 543, 2011.

[2] J. Lloyd-Hughes and T.-I. Jeon, "A review of the terahertz conductivity of bulk and nano-materials," *J. Infrared Millim. THz Waves*, vol. 33, p. 871, 2012.

[3] H. Němec, P. Kužel, and V. Sundström, "Charge transport in nanostructured materials for solar energy conversion studied by time-resolved terahertz spectroscopy," *J. Photochem. Photobiol. A*, vol. 215, p. 123, 2010.

[4] L. Fekete, P. Kužel, H. Němec, F. Kadlec, A. Dejneka, J. Stuchlík, and A. Fejfar, "Ultrafast carrier dynamics in microcrystalline silicon probed by time-resolved terahertz spectroscopy," *Phys. Rev. B*, vol. 79, p. 115306, 2009.

[5] D. G. Cooke, A. N. Macdonald, A. Hryciw, J. Wang, Q. Li, A. Meldrum, and F. A. Hegmann, "Transient terahertz conductivity in photoexctied silicon nanocrystal films," *Phys. Rev. B*, vol. 73, p. 193311, 2006.

[6] D. G. Cooke, A. Meldrum, and P. Uhd Jepsen, "Ultrabroadband terahertz conductivity of Si nanocrystal films," *Appl. Phys. Lett.*, vol. 101, p. 211107, 2012.

[7] F. A. Hegmann, O. Ostroverkhova, and D. G. Cooke, *Photophysics of Molecular Materials*. Weinheim, Germany: Wiley-VCH Verlag, 2006, pp. 367–428.

[8] P. A. George, J. Strait, J. Dawlaty, S. Shivaraman, M. Chandrashekhar, F. Rana, and M. G. Spencer, "Ultrafast optical-pump terahertz-probe spectroscopy of the carrier relaxation and recombination dynamics in epitaxial graphene," *Nano Lett.*, vol. 8, p. 4248, 2008.

[9] H. Němec, J. Rochford, O. Taratula, E. Galoppini, P. Kužel, T. Polívka, A. Yartsev, and V. Sundström, "Influence of the electron-cation interaction on electron mobility in dye-sensitized ZnO and TiO_2 nanocrystals: A study using ultrafast terahertz spectroscopy," *Phys. Rev. Lett.*, vol. 104, p. 197401, 2010.

[10] H. Němec, E. Galoppini, H. Imagori, and V. Sundström, "Solar energy conversion—Natural to artificial," in *Comprehensive Nanosci. Technol.*, D. L. Andrews, G. D. Scholes, and G. P. Wiederrecht, Eds. Oxford, U.K.: Academic, 2011, vol. 2, pp. 325–359.

[11] P. Uhd Jepsen, D. G. Cooke, and M. Koch, "Terahertz spectroscopy and imaging—Modern techniques and applications," *Laser Photon. Rev.*, vol. 5, p. 124, 2011.

[12] P. Kužel, F. Kadlec, and H. Němec, "Propagation of terahertz pulses in photoexcited media: Analytical theory for layered systems," *J. Chem. Phys.*, vol. 127, p. 024506, 2007.

[13] H.-K. Nienhuys and V. Sundstörm, "Influence of plasmons on terahertz conductivity measurements," *Appl. Phys. Lett.*, vol. 87, p. 012101, 2005.

[14] M. C. Beard, G. M. Turner, and C. A. Schmuttenmaer, "Transient photoconductivity in GaAs as measured by time -resolved terahertz spectroscopy," *Phys. Rev. B*, vol. 62, p. 15764, 2000.

[15] N. V. Smith, "Classical generalization of the Drude formula for the optical conductivity," *Phys. Rev. B*, vol. 64, p. 155106, 2001.

[16] D. G. Cooke, A. N. MacDonald, A. Hryciw, A. Meldrum, J. Wang, Q. Li, and F. A. Hegmann, "Ultrafast terahertz conductivity of photoexcited nanocrystalline silicon," *J. Mater. Sci.: Mater. Electron.*, vol. 18, p. S447, 2007.

[17] H. Němec, P. Kužel, and V. Sundström, "Far-infrared response of free charge carriers localized in semiconductor nanoparticles," *Phys. Rev. B*, vol. 79, p. 115309, 2009.

[18] Z. Mics, H. Němec, I. Rychetský, P. Kužel, P. Formánek, P. Malý, and P. Němec, "Charge transport and localization in nanocrystalline CdS films: A time-resolved terahertz spectroscopy study," *Phys. Rev. B*, vol. 83, p. 155326, 2011.

[19] J. Mrozek and H. Němec, "Calculation of terahertz conductivity spectra in semiconductors with nanoscale modulation," *Phys. Rev. B*, vol. 86, p. 075308, 2012.

[20] L. V. Titova, T. L. Cocker, D. G. Cooke, X. Wang, A. Meldrum, and F. A. Hegmann, "Ultrafast percolative transport dynamics in silicon nanocrystal films," *Phys. Rev. B*, vol. 83, p. 085403, 2011.

[21] G. M. Turner, M. C. Beard, and C. A. Scmuttenmaer, "Carrier localization and cooling in dye-sensitized nanocrystalline titanium dioxide," *J. Phys. Chem. B*, vol. 106, p. 11716, 2002.

[22] J. B. Baxter and C. A. Schmuttenmaer, "Conductivity of ZnO nanowires, nanoparticles, and thin films using time-resolved terahertz spectroscopy," *J. Phys. Chem. C*, vol. 110, p. 25229, 2006.

[23] F. Hecht and O. Pironneau, *FreeFem++*. Paris, France: Univ. Pierre et Marie Curie, 2007.

[24] I. Rychetský and A. Klíč, "Dielectric response of arbitrary-shaped clusters studied by the finite element method," *Ferroelectrics*, vol. 427, p. 143, 2012.

[25] D. J. Bergman, "The dielectric constant of a composite material—A problem in classical physics," *Phys. Rep.*, vol. 43, p. 377, 1978.

[26] J. Petzelt, I. Rychetský, and D. Nuzhnyy, "Dynamic ferroelectric-like softening due to the conduction in disordered and inhomogeneous systems: Giant permittivity phenomena," *Ferroelectrics*, vol. 426, p. 171, 2012.

[27] J. Sturm, P. Grosse, and W. Theiss, "Effective dielectric functions of alkali halide composites and their spectral representation," *Z. Phys. B Condensed Matter*, vol. 83, p. 361, 1991.

[28] E. Hendry, M. Koeberg, B. O'Regan, and M. Bonn, "Local field effects on electron transport in nanostructured TiO_2 revealed by terahertz spectroscopy," *Nano Lett.*, vol. 6, p. 755, 2006.

[29] S. A. Jensen, H. Němec, I. Rychetský, E. Hendry, K.-J. Tielrooij, and M. Bonn, "Transient terahertz response of films of TiO_2 micro- and nano-particles," , unpublished.

[30] L. Forro, O. Chauvet, D. Emin, L. Zuppiroli, H. Berger, and F. Lévy, "High mobility n-type charge carriers in large single crystals of anatase (TiO_2)," *J. Appl. Phys.*, vol. 75, p. 633, 1994.

[31] J. C. Dyre, "The random free-energy barrier model for ac conduction in disordered solids," *J. Appl. Phys.*, vol. 64, p. 2465, 1988.

[32] H. Němec, Z. Mics, M. Kempa, P. Kužel, O. Hayden, Y. Liu, T. Bein, and D. Fattakhova-Rohlfing, "Tuning the conduction mechanism in niobium-doped titania nanoparticle networks," *J. Phys. Chem. C*, vol. 115, p. 6968, 2011.

[33] R. J. Gonzalez, R. Zallen, and H. Berger, "Infrared reflectivity and lattice fundamentals in anatase TiO2," *Phys. Rev. B*, vol. 55, p. 7014, 1997.

[34] G. M. Turner, M. C. Beard, and C. A. Schmuttenmaer, "Carrier localization and cooling in dye-sensitized nanocrystalline titanium dioxide," *J. Phys. Chem. B*, vol. 106, p. 11716, 2002.

[35] H. Němec, P. Kužel, F. Kadlec, D. Fattakhova-Rohlfing, J. Szeifert, T. Bein, V. Kalousek, and J. Rathouský, "Ultrafast terahertz photoconductivity in nanocrystalline mesoporous TiO_2 films," *Appl. Phys. Lett.*, vol. 96, p. 062103, 2010.

[36] V. Zajac, H. Němec, C. Kadlec, P. Kužel, K. Kůsová, and I. Pelant, "Electron transport in silicon nanocrystals studied by time-resolved THz spectroscopy," , unpublished.

[37] K. Ghosh and R. Fuchs, "Spectral theory for two-component porous media," *Phys. Rev. B*, vol. 38, p. 5222, 1988.

[38] C. Pecharromán and F. J. Gordillo-Vázquez, "Expansion of the spectral representation function of a composite material in a basis of Legendre polynomials: Experimental determination and analytic approximations," *Phys. Rev. B*, vol. 74, p. 035120, 2006.

[39] J. Schuster, G. He, B. Mandlmeier, T. Yim, K. T. Lee, T. Bein, and L. F. Nazar, *Angew. Chem.*, vol. 124, p. 3651, 2012.

[40] S. Ito, T. N. Murakami, P. Comte, P. Liska, C. Grätzel, M. K. Nazeeruddin, and M. Grätzel, *Thin Solid Films*, vol. 516, p. 4613, 2008.

H. Němec, photograph and biography not available at time of publication.

V. Zajac, photograph and biography not available at time of publication.

I. Rychetský, photograph and biography not available at time of publication.

D. Fattakhova-Rohlfing, photograph and biography not available at time of publication.

B. Mandlmeier, photograph and biography not available at time of publication.

T. Bein, photograph and biography not available at time of publication.

Z. Mics, photograph and biography not available at time of publication.

P. Kužel, photograph and biography not available at time of publication.